ADVANCED FUNCTIONAL MATERIALS
www.afm-journal.de

The Unique Structural Evolution of the O3-Phase $Na_{2/3}Fe_{2/3}Mn_{1/3}O_2$ during High Rate Charge/Discharge: A Sodium-Centred Perspective

Neeraj Sharma, Elena Gonzalo, James C. Pramudita, Man Huon Han, Helen E. A. Brand, Judy N. Hart, Wei Kong Pang, Zaiping Guo, and Teófilo Rojo**

The development of new insertion electrodes in sodium-ion batteries requires an in-depth understanding of the relationship between electrochemical performance and the structural evolution during cycling. To date in situ synchrotron X-ray and neutron diffraction methods appear to be the only probes of in situ electrode evolution at high rates, a critical condition for battery development. Here, the structural evolution of the recently synthesized O3-phase of $Na_{2/3}Fe_{2/3}Mn_{1/3}O_2$ is reported under relatively high current rates. The evolution of the phases, their lattice parameters, and phase fractions, and the sodium content in the crystal structure as a function of the charge/discharge process are shown. It is found that the O3-phase persists throughout the charge/discharge cycle but undergoes a series of two-phase and solid-solution transitions subtly modifying the sodium content and atomic positions but keeping the overall space-group symmetry (structural motif). In addition, for the first time, evidence of a structurally characterized region is shown that undergoes two-phase and solid-solution phase transitions simultaneously. The Mn/Fe–O bond lengths, *c* lattice parameter evolution, and the distance between the Mn/FeO_6 layers are shown to concertedly change in a favorable manner for Na^+ insertion/extraction. The exceptional electrochemical performance of this electrode can be related in part to the electrode maintaining the O3-phase throughout the charge/discharge process.

1. Introduction

Li-ion batteries (LIBs) have long been the focus of the secondary battery industry due to their large specific capacity and high operating voltage; most of the current small- to medium-size mobile electronic devices use some form of LIB.[1] However, expanding the use of LIB to stationary applications may not be realistic due to the uncertainty regarding the distribution and availability of Li sources.[2] Recently, Na-ion batteries (NIBs) have been receiving tremendous attention because Na is one of the most abundant elements in the Earth's crust and seawater,[3] and also is the second lightest alkali metal after Li. Therefore, NIBs could be an excellent complement to LIBs in applications where energy density per unit measure is not so critical.

Among many cathode candidates, layered oxides of general formula $Na_xM_TO_2$ (M_T = Ti, V, Cr, Mn, Fe, Co, Ni, and mixtures of 2–3 of these elements) have been investigated extensively because of their

Dr. N. Sharma, J. C. Pramudita
School of Chemistry
UNSW Australia
Sydney, NSW 2052, Australia
E-mail: Neeraj.sharma@unsw.edu.au
Dr. E. Gonzalo, Dr. M. H. Han, Prof. T. Rojo
CICenergigune
Parque Tecnológico de Álava
Albert Einstein 48, ED.CIC, 01510 Miñano, Spain
E-mail: trojo@cicenergigune.com
Dr. H. E. A. Brand
Australian Synchrotron
Clayton, Victoria 3168, Australia
Dr. J. N. Hart
School of Materials Science and Engineering
UNSW Australia
Sydney, NSW 2052, Australia

DOI: 10.1002/adfm.201501655

Dr. W. K. Pang, Prof. Z. Guo
School of Mechanical, Materials, and Mechatronic Engineering
Institute for Superconducting & Electronic Materials
Faculty of Engineering
University of Wollongong
NSW 2522, Australia
Dr. W. K. Pang
Australian Nuclear Science and Technology Organisation Locked Bag 2001
Kirrawee DC, NSW 2232, Australia
Prof. T. Rojo
Departamento de Química Inorgánica
Universidad del País Vasco UPV/EHU
P.O. Box. 644, 48080 Bilbao, Spain

high theoretical capacity and the potential to select relatively inexpensive transition metals.[4] In fact, the first Na intercalation chemistry was demonstrated with a layered oxide[5] and both single or combinations of many M_T have been investigated over last decades.[6] Layered oxides are typically classified by Na environment and oxide layer stacking. In the P2-phase, trigonal prismatically coordinated Na ions are sandwiched between M_TO_6 oxide layers that follows an AABB stacking order; in the O3-phase, octahedrally coordinated Na ions are located in between the oxide layers that follow an ABCABC stacking order.[7]

Normally, the P2-phase is synthesized with Na ≅ 0.7 while the O3-phase is synthesized with Na ≅ 1.0. The P2-phase with initial Na content ≲ 0.7 does not typically undergo phase transitions until Na ≲ 0.33[8] while the fully sodiated O3-phase undergoes complex phase transitions during cycling.[6c] Thus, the P2-phase maintains its structural stability during cycling until the highly desodiated state and therefore generally exhibits better overall electrochemical performance than the O3-phase.[9] However, successful synthesis of pure P2- and O3-phase, both with an initial Na content of 2/3, has demonstrated that the overall electrochemical performance of both phases at all tested cycling rates, including high rates, are almost identical.[9] Interestingly, in situ X-ray diffraction (XRD) experiments at a lower cycling rate indicate that the O3-phase with an initial Na content of 2/3 undergoes multiple phase transitions during electrochemical cycling similar to fully sodiated O3-phase, but these transitions are not exceptionally obvious on the cyclic profile as multiple potential plateau type behavior, especially at higher rates. Thus there appears to be a contradiction between the potential profile of the O3-phase which indicates good phase stability and electrochemical performance equivalent to the P2-phase, and the in situ electrode structure measured during cycling at a low rate (C/20), which indicates poor phase stability.

To resolve this contradiction, it is necessary to perform in situ structural characterization at relatively high cycling rates. It is important to note that only a few techniques can probe batteries in situ in a nondestructive manner and of these a smaller number of techniques can do so sufficient time-resolution to examine high rate cycling, to date only neutron powder and synchrotron X-ray powder diffraction. Ex situ or low-rate in situ diffraction methods show electrode structure at equilibrium or quasi-equilibrium conditions, they do not represent the electrode structure at moderate or high rates. In situ methods with sufficient time-resolution to capture data in short enough intervals with sufficient resolution and quality can be used for structural analysis at high current rates.[10] For sodium-ion batteries for high-rate, nondesctructive structural information this essentially means in situ synchrotron X-ray diffraction for now. In principle, with sufficient resolution almost all structural parameters can be determined for the electrode in question.[11]

Therefore, we present here a time-resolved in situ synchrotron XRD study of the relatively new O3-phase $Na_{2/3}Fe_{2/3}Mn_{1/3}O_2$ to understand the relationship between the observed electrochemical performance and the crystal structure evolution. We highlight the phase transitions and sodium evolution that occur during electrochemical cycling. Crucially we have performed these measurements at a high current rate, C/2.5, thus providing one of the first high-rate insights into this family of layered materials that has strong potential for cathodes in commercial batteries.

2. Results and Discussion

2.1. Overall Evolution

The phase evolution during entire charge/discharge process occurs by a combination of solid solution and two-phase reactions. The changes in the reflection position (2θ-value) with time are shown in **Figure 1**, for the 003, 006, 101, 10–2, 107, and 10–8 reflections in the O3 setting; the regions where two phases are present and the phase fractions are changing are indicated with orange shading.[12] Notably the changes in the 2θ-values of the

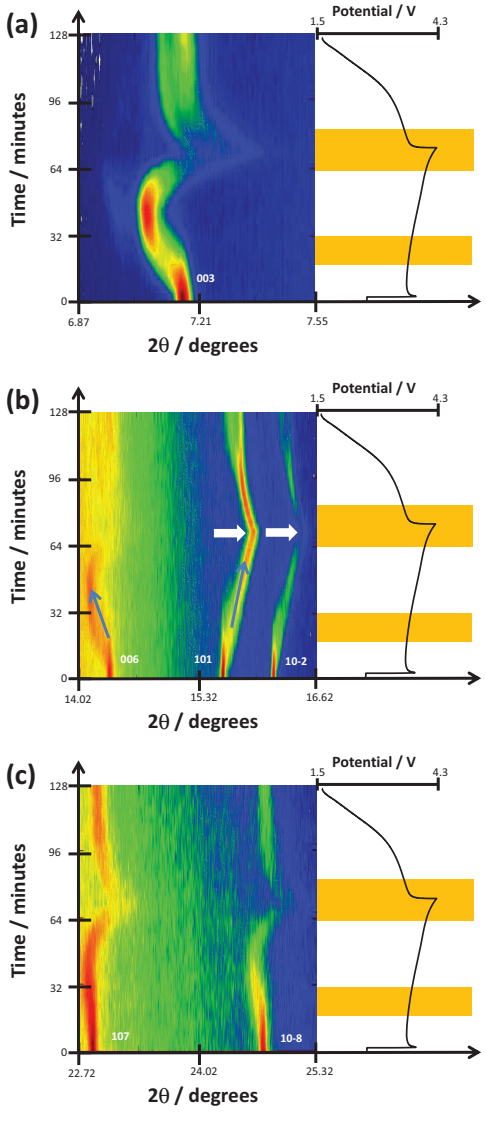

Figure 1. Selected 2θ regions of in situ synchrotron XRD data highlighting the evolution of the a) 003, b) 006, 101, 10–2, and c) 107 and 10–8 reflections by a color scale and the potential profile (right). The orange shaded boxes highlight regions where two phases are present, indicated by the disappearance and appearance of reflections.

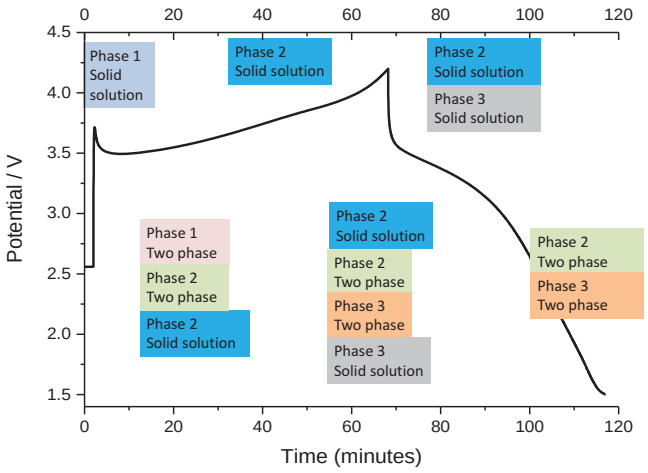

Figure 2. The phases present and reactions they are undergoing in the $Na_{0.622(6)}Fe_{2/3}Mn_{1/3}O_2$ cathode during charge and discharge.

003 and 006 reflections are the opposite of the changes in the 101 and 10–2 reflections during charge (and discharge), e.g., as the 003 and 006 2θ-values decrease, the 101 and 10–2 2θ-values increase, as shown by the blue arrows in Figure 1b. This suggests an anisotropic evolution of the lattice parameters. Additionally, comparing the 101 and 10–2 reflections at the charged state, there is a distinct increase in intensity of the 101 compared to the 10–2 reflection as indicated by the white arrows in Figure 1b.

Considering the entire charge/discharge cycle probed in this experiment, the structural evolution observed can be described as shown in **Figure 2**. There are at least three phases that evolve during this process. Below, the phase formation and evolution is discussed for each of these three phases with respect to the electrochemical curve. In addition, further electrochemical data can be found in the Supporting Information (Figures S1 and S2, Supporting Information).

2.2. Initial Structure

The initial O3 model using the "O and P-type" definition of these layered phases[7,12] was refined using the in situ synchrotron XRD data of the electrode in the coin cell. The crystal structure adopted *R*-3*m* symmetry and the refined lattice parameters were a = 2.96256(2), c = 16.4902(2) Å (crystallographic details can be found in **Table 1** and the fit is shown in **Figure 3**). These values for the lattice parameters are slightly different from those found from the pure powders of a = 2.9905(1), c = 16.2602(9) Å; however, our structural model represents the material inside a battery, in contact with electrolyte, and thus some exchange (Na loss/gain) may occur as discussed in our previous work.[11c,13] The sodium occupation (site occupancy factors or SOFs) and the atomic displacement parameters (ADPs) correlated to a certain extent and therefore were refined sequentially to obtain the model shown in Table 1. For the refinements, reflections arising from the aluminum current collector and sodium anode were excluded as their positions did not overlap with many cathode reflections. As a direct comparison, laboratory XRD data collected on pristine electrodes for 0.5 and 1 h are shown and discussed in the Supporting Information (Figure S3). This clearly shows the significantly higher signal-to-noise of the data obtained using the in situ setup.

Table 1. Refined crystallographic parameters for $Na_{0.622(6)}Fe_{2/3}Mn_{1/3}O_2$.

Atom	Wyckoff	x	y	z	SOF[a)]	Isotropic ADP[a)] [×100)/Å^2]
Na	3	0	0	0	0.622(6)	7.05[b)]
Mn	3	0	0	0.5	1/3	7.86[b,c)]
Fe	3	0	0	0.5	2/3	7.86[b,c)]
O	6	0	0	0.2350(3)	1	7.63[b)]

[a)]Atomic displacement parameter (ADP), site occupancy factor (SOF); [b)]Refined alternatively to SOFs and fixed when convergence was achieved; [c)]Constrained to be equal. Space group = *R*-3*m*, 33 refinement parameters, χ^2 = 1.43, R_p = 1.66%, wRp = 2.17%, a = 2.96256(2), c = 16.4902(2) Å.

2.3. Evolution on Initial Charge

On initial charge, there is a solid solution reaction of the initial phase, which we refer to as Phase 1. The next structural transition during charge is the formation of a second phase; a two-phase region, where both of these phases are present, occurs from 11 to 28.8 min or 3.50 to 3.62 V (indicated by the orange box in Figure 1). Using stacked plots (**Figure 4**a), the similarity of the two-phases becomes more apparent as does their evolution. The 003 reflection of the original phase disappears while the peak for the 2nd phase (Phase 2) appears and simultaneously begins to change in 2θ-value, which indicates that simultaneous

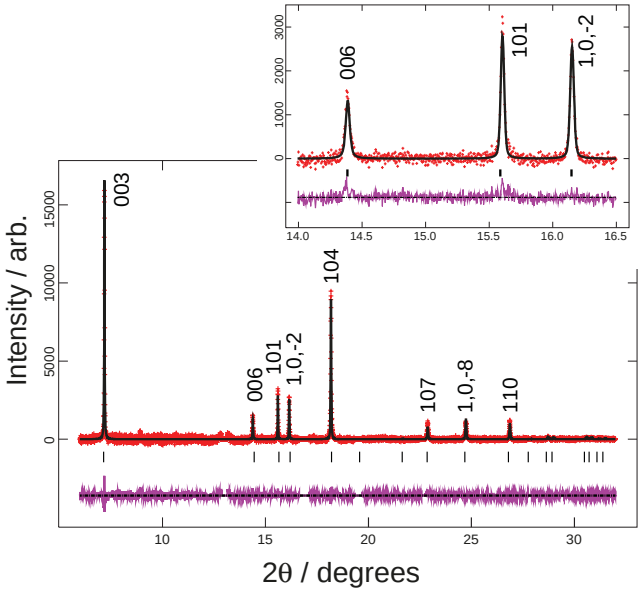

Figure 3. Rietveld refined fit of the $Na_{0.622(6)}Fe_{2/3}Mn_{1/3}O_2$ model to the initial in situ synchrotron XRD dataset. Data are shown as crosses, the calculated Rietveld model as a line through the data, and the difference between the data and the model as the line below the data. The vertical reflection markers are for O3- $Na_{0.622(6)}Fe_{2/3}Mn_{1/3}O_2$ and a zoomed in section, 14 ≤ 2θ ≤ 16.5, is shown.

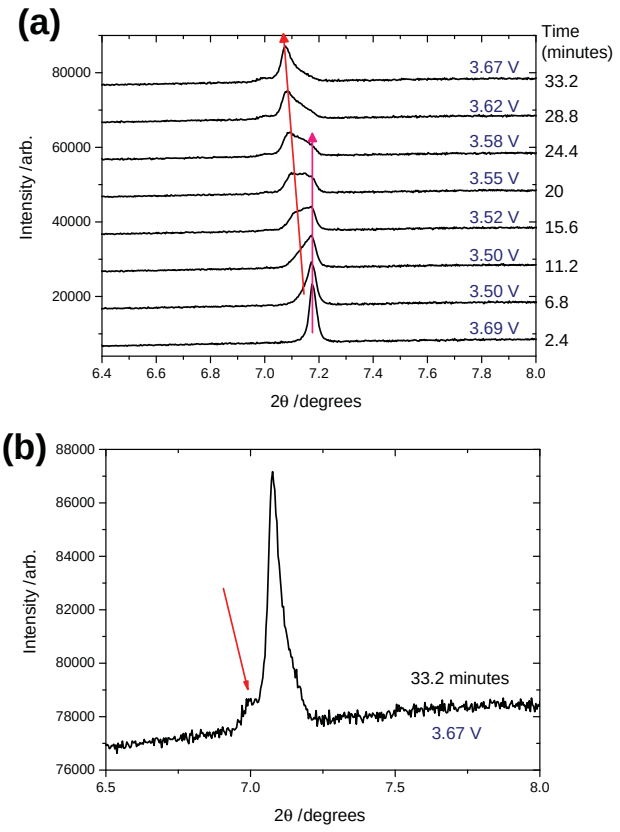

Figure 4. a) Snapshots via a stacked plot of the in situ synchrotron XRD data of the 003 reflections with the time and potential listed. The purple arrow indicates the disappearance of reflections from initial phase (Phase 1) and red arrow the appearance of new reflections from Phase 2 which also show changes in 2θ-value during the same region. b) A zoomed in region of the Phase 2 003 reflection showing the possible monoclinic O1 phase as reported in the literature.[13]

two-phase and solid solution reactions are occurring.[10d] Similar simultaneous reactions have been previously observed in $LiFePO_4$ cathodes by in situ neutron powder diffraction experiments on lithium-ion cells.[10d] Thus the lattice parameters of Phase 2 can be modeled whilst the two phase reaction is occurring. The lattice parameters of Phase 1 do not change, as evidenced by a static 2θ-value during this two-phase region, so these values were held constant during fitting. Phase 1 disappears at approximately 33.2 min or 3.67 V into charge.

The diffraction pattern at 33.2 min or 3.67 V also shows a minute feature at a slightly lower 2θ-value with respect to the Phase 2 003 reflection (Figure 4b). This feature appears at ≈24 min or 3.58 V into charge and persists until the charged state. On initial observation, this appears to be another phase in this region, which we tentatively attribute to the monoclinic phase that has been described in the literature for related layered structures (e.g., O1-monoclinic).[14]

The Phase 2 lattice parameter and sodium content evolve during the simultaneous reaction region, with the evolution continuing past this region by a solid solution reaction (change in reflection 2θ-value). The dataset in the solid solution reaction regime of Phase 2 at 33.2 min (3.67 V, Figure 4b) was used to model its structure. Various models were used encompassing

Table 2. Refined crystallographic parameters for $Na_{0.457(11)}Fe_{2/3}Mn_{1/3}O_2$.

Atom	Wyckoff	*x*	*y*	*z*	SOF[a)]	Isotropic ADP[a)] [×100)/Å^2]
Na	3	0	0	0	0.457(11)	7.05[b)]
Mn	3	0	0	0.5	1/3	7.86[b,c)]
Fe	3	0	0	0.5	2/3	7.86[b,c)]
O	6	0	0	0.2340(5)	1	7.63[b)]

[a)]Atomic displacement parameter (ADP), site occupancy factor (SOF); [b)]Fixed from Phase 1; [c)]Constrained to be equal. Space group = *R*-3*m*, 33 refinement parameters, $\chi^2 = 1.52$, $R_p = 1.74\%$, wRp = 2.36%, $a = 2.9314(1)$, $c = 16.7241(5)$ Å.

the possible options, such as those adopting *Cmcm* and $P6_3/mmc$ symmetry, but there were inconsistencies with these models (e.g., unmatched or missing reflections). Note the expected P3 model was trialed but the fit did not converge and overall was poorly modeling the data.[9,14] The *R*-3*m* model (O3-like) still provided the best fit to the data, with the lattice parameters merely expanded in *c* and reduced in *a*, the sodium content reduced and a slight decrease in the oxygen positional parameter. The details of the refined O3-like structural model are shown in **Table 2** and the fit to the data in **Figure 5** (dataset corresponding to 33.2 min or 3.67 V, Figure 4b). The inset in Figure 5 shows an expanded view of the 003 reflection in the *R*-3*m* setting; relative to the Phase 2 peak, a small feature can be seen at higher angle associated with Phase 1, while the feature at lower angle (indicated by an arrow in Figure 5 inset) may be associated with the monoclinic O1 phase.[14a] Unfortunately, there are not enough reflections to fully characterize this monoclinic phase.

Refinements were performed on models for Phase 2 with varying ADPs resulting in similar models which did not significantly reduce the statistics of the fit. Hence, to limit the number

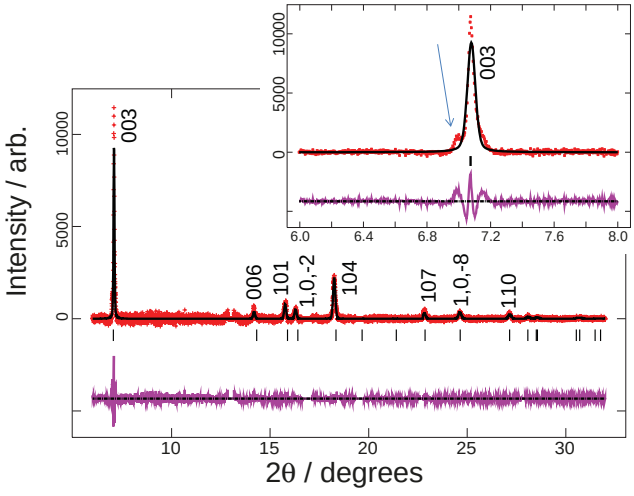

Figure 5. Rietveld refined fit of the $Na_{0.457(11)}Fe_{2/3}Mn_{1/3}O_2$ model to the in situ synchrotron XRD dataset at 33.2 min or 3.67 V. Data are shown as crosses, the calculated Rietveld model as a line through the data, and the difference between the data and the model as the line below the data. The vertical reflection markers are for O3-$Na_{0.457(11)}Fe_{2/3}Mn_{1/3}O_2$ and a zoomed in section highlighting the 003 reflection and the possible monoclinic phase is indicated by the arrow.

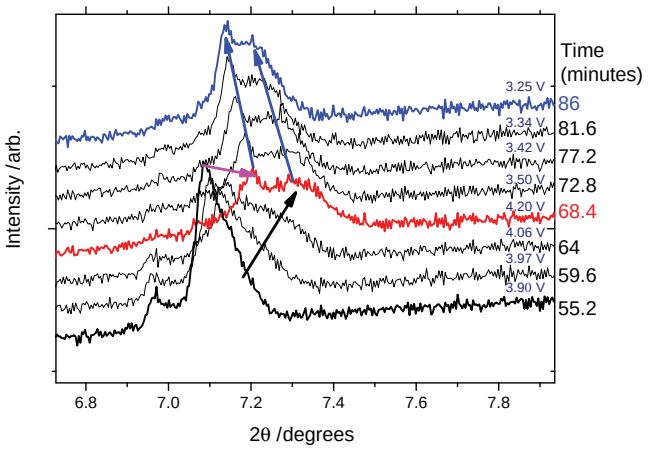

Figure 6. Snapshots via a stacked plot of the in situ synchrotron XRD data of the 003 reflections with the time and potential listed. The red pattern corresponds to the end of the simultaneous reaction mechanism region and the charged state. The black arrow indicates the appearance of new reflections from Phase 3 and these new reflections show changes in 2θ-value during the same region. The magenta arrow indicates the disappearance of reflections from Phase 2 and these reflections show changes in 2θ-value during the same region. The blue arrows indicate the simultaneous presence of Phases 2 and 3 and changes in their 2θ-value but minimal if any changes in the phase ratio (relative intensity).

of variables in each dataset, the ADPs were fixed to the original values found in Phase 1 for all subsequent refinements. Therefore, both Phase 1 and Phase 2 can be modeled with *R*-3*m* symmetry and show variations in the lattice parameters, sodium content, and oxygen positions. If the *R*-3*m* model persists during charging, the intensity fluctuations of the 101 and 10–2 reflections (indicated with white arrows in Figure 1b) are likely to be related to the changing sodium content or oxygen positional parameter, as will be detailed below.

2.4. The Charged State and Initial Discharge

Closer to the charged state (i.e., from ≈55 min or 3.90 V to fully charged), we find another interesting series of phase transitions. For clarity the 003 reflection is used to highlight these changes in **Figure 6**. Phase 2 continues to undergo a solid solution reaction, with the reflection intensities decreasing and the lattice parameters changing, as shown by the changes in the 2θ value of the 003 reflection (Figure 6). Simultaneously another phase appears, indicated by a high angle (smaller lattice parameter) reflection, which is referred to as Phase 3; the intensity of the peaks associated with this phase increases while the 2θ value of the reflection changes (lattice changes). This is another simultaneous two-phase and solid solution reaction where both phases undergo changes in both lattice parameters and reflection intensity. However, unlike the previous simultaneous reaction region, where Phase 1 and Phase 2 coexisted but the lattice of only Phase 2 was changing, in this case both phases are active in lattice and phase fraction evolution (see black and magenta arrows in Figure 6). In other words, both phases are changing simultaneously in a two-phase and solid solution manner. Such an observation

Table 3. Refined crystallographic parameters for Phase 2, $Na_{0.34(4)}Fe_{2/3}Mn_{1/3}O_2$, and Phase 3, $Na_{0.18}Fe_{2/3}Mn_{1/3}O_2$, charged state (68.4 min, 4.20 V).

Atom	Wyckoff	*x*	*y*	*z*	SOF[a]	Isotropic ADP[a] [×100)/Å^2]
Phase 2						
Na	3	0	0	0	0.34(4)	17.1[b]
Mn	3	0	0	0.5	1/3	7.86[b,c]
Fe	3	0	0	0.5	2/3	7.86[b,c]
O	6	0	0	0.252(1)	1	7.63[b]
Phase 3						
Na	3	0	0	0	0.18[d]	–
Mn	3	0	0	0.5	1/3	7.92[b,c]
Fe	3	0	0	0.5	2/3	7.92[b,c]
O	6	0	0	0.251(1)	1	7.49[b]

[a]Atomic displacement parameter (ADP), site occupancy factor (SOF); [b]Refined alternatively to SOFs and fixed; [c]Constrained to be equal; [d]Fixed according to refinements. Space group = *R*-3*m*, 37 refinement parameters, χ^2 = 1.46, R_p = 1.76%, wRp = 2.28%, Phase 2 *a* = 2.9040(3), *c* = 16.437(2) Å and weight fraction 57.6(9)% and Phase 3 *a* = 2.8992(4), *c* = 16.192(2) Å and weight fraction 42.4(6)%.

to the best of the authors' knowledge is unprecedented in the literature. This reaction occurs between 55.2 and 68.4 min or 3.90 and 4.20 V on charge.

Toward the end of this simultaneous reaction region (≈68.4 min, 4.20 V the charged state, Figure 6), the phase fractions appear to stabilize and then both phases undergo a solid solution reaction (Phase 2 and Phase 3). An alternative explanation for this behavior is the presence of a more complex lower symmetry structure near the charged state. Thus, the two reflections in this region depicted in Figure 6 may belong to a single lower symmetry phase and these reflections change in intensity as the sodium content changes. However, no structural model with two reflections near the 003 reflection (with the 003 reflection defined in the *R*-3*m* setting) exists, so the phases at the charged state may need further characterization.

Due to the complexity of the phase evolution near the charged state, the last data set in the entire experiment (discharged) was modeled first with Phases 2 and 3, as it shows the same phase composition as the charged state. Using this, the charged state was modeled in conjunction with the results already presented for Phase 2. Note again other models were attempted but the O3 model(s) appeared to provide the best fits for both Phase 2 and Phase 3. **Tables 3** and 4 detail the crystal structure and phase distribution at the charged to 4.20 V and the discharged to 1.50 V states, respectively. **Figures 7** and **8** show the fits of the structural model to the data at these points.

The results indicate that the Na content at the charged state is low, but the fitting is quite insensitive to the Na content, so it is difficult to determine the exact Na content solely from the structural refinement. Computational results discussed later suggest that a Na content of at least ≈0.18 is required to maintain structural stability. Therefore, a Na content of 0.18 was used for the refinement of Phase 3 in the charged state.

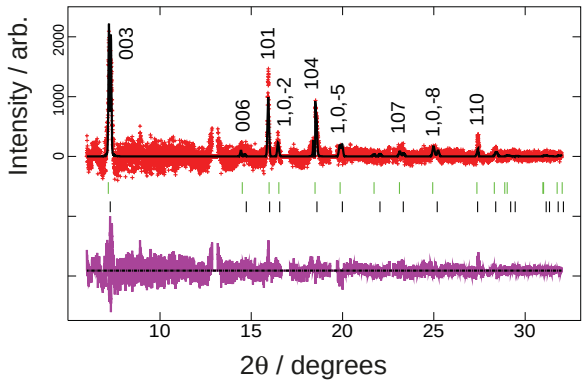

Figure 7. Rietveld refined fit of Phase 2, $Na_{0.43(4)}Fe_{2/3}Mn_{1/3}O_2$, and Phase 3, $Na_{0.18}Fe_{2/3}Mn_{1/3}O_2$, models to the in situ synchrotron XRD data at the charged state (68.4 min, 4.20 V). Data are shown as crosses, the calculated Rietveld model as a line through the data, and the difference between the data and the model as the line below the data. The vertical reflection markers are for (top) Phase 2, $Na_{0.43(4)}Fe_{2/3}Mn_{1/3}O_2$, and (bottom) Phase 3, $Na_{0.18}Fe_{2/3}Mn_{1/3}O_2$.

2.5. Discharge

The phases present and their distribution (e.g., the sequence of reaction mechanisms) on discharge appears to be different from charge, with the two phase mixture of Phases 2 and 3 remaining throughout the discharge; both phases have similar lattice parameters and undergo subtle reactions. The discharge process is shown in more detail in **Figure 9**. For the 003 reflection there is a noticeable increase in Phase 3,

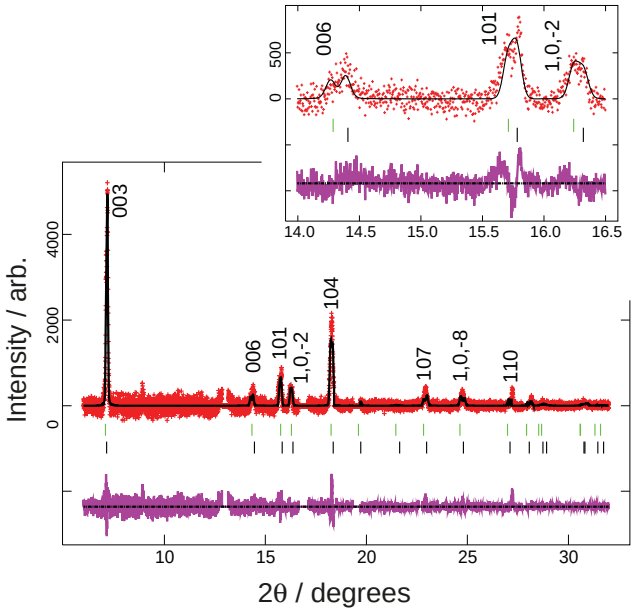

Figure 8. Rietveld refined fit of the Phase 2, $Na_{0.80(3)}Fe_{2/3}Mn_{1/3}O_2$, and Phase 3, $Na_{0.52(2)}Fe_{2/3}Mn_{1/3}O_2$, models to the last in situ synchrotron XRD dataset during discharge (121 min, 1.50 V). Data are shown as crosses, the calculated Rietveld model as a line through the data, and the difference between the data and the model as the line below the data. The vertical reflection markers are for (top) Phase 2, $Na_{0.80(3)}Fe_{2/3}Mn_{1/3}O_2$, and (bottom) Phase 3, $Na_{0.52(2)}Fe_{2/3}Mn_{1/3}O_2$.

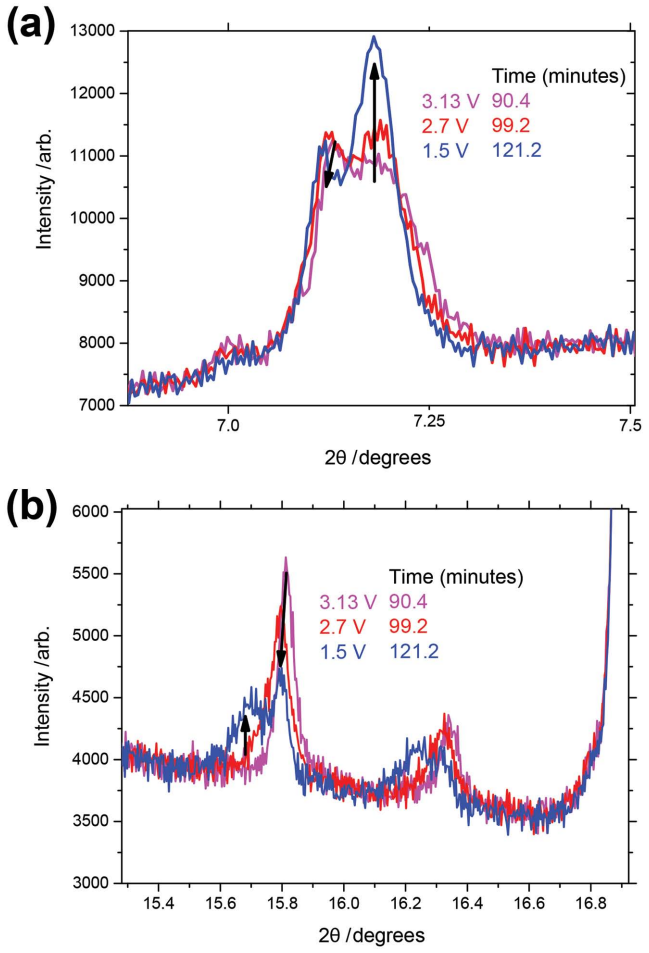

Figure 9. Snapshots via a stacked plot of the in situ synchrotron XRD data of the a) 003, b) 101 and 10–2 reflections with the time during discharge. The black arrows indicate the enhancement of reflections associated with Phase 3 and the decrease (or subtle changes) of reflections associated with Phase 2.

higher angle, reflection intensity, and a subtle change in the lower angle reflection associated with Phase 2. The 101 and 10–2 reflections show similar behavior with the increase of reflection intensities (shown as arrows in Figure 9) associated with Phase 3. Additionally, the 101 and 10–2 reflections for Phase 2 decrease in intensity during discharge, which again may be associated with either change in the phase fractions or in the structural parameters, e.g., sodium content. The latter is more likely to result in changes in the lattice parameters (i.e., removal/insertion of sodium requires the cell to contract/expand); however, changes in the lattice parameters are not clearly evident in these data on discharge, so the two-phase reaction appears to be the major contributor to changes in the reflection intensities during discharge.

It is interesting to note that the phase evolution is very different on discharge than charge. Phases 2 and 3 are maintained in the structure throughout the discharge, with only their phase fractions changing.

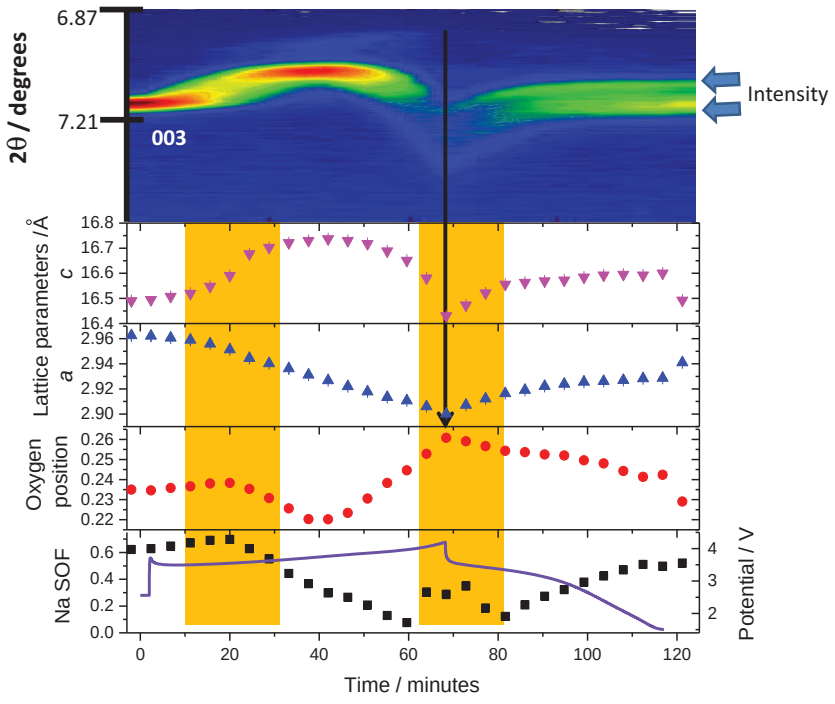

Figure 10. A crude single phase picture of the evolution of the $Na_{0.622(6)}Fe_{2/3}Mn_{1/3}O_2$ electrode during charge/discharge. (Top) Selected 2θ regions of in situ synchrotron XRD data highlighting the evolution of the 003 reflections by a color scale. The *c* (purple triangles) and *a* (blue triangles) lattice parameters, oxygen positional parameter (red circles), sodium SOF (black squares), and the potential profile. The orange shaded box highlights obvious two-phase regions as mentioned in Figure 1 but found to be more complex.

2.6. Structural Analysis

To determine the overall structural evolution during battery function, we note that there are at least 4–5 phase transitions (Figure 1) and that structural models for each of these phases need to be determined and sequentially refined in the respective regions. The phase fractions are the appropriate measure of electrode evolution in the two-phase regions, while both lattice parameters and sodium content can be tracked in solid solution regions (see our previous work in this area).[10d,11] Interestingly, in this case, we have regions with simultaneous solid solution and two-phase electrode evolution so the phase fractions can be followed in addition to the lattice and sodium content of at least one phase.

However, prior to discussing the details of these reactions, we present a simple sequential refinement using a single O3 structural model and allowing the lattice, sodium SOF, oxygen positional parameter, scale and background to refine for the entire in situ synchrotron XRD data series. The results are shown in **Figure 10** and the refinement does approximate a number of subtle structural features. The Na content decreases and increases in pseudo-single phase regions. The trends in the *a* and *c* lattice parameters appear as expected (in comparison to changes seen in the 003 reflection for *c* and Figure 1 for *a*), with the *a* lattice parameter decreasing during charging and the *c* parameter increasing to a maximum and then decreasing. Maxima in the *c* lattice parameter are often observed in in situ data for layered cathodes used in lithium ion batteries.[15] The oxygen positional parameter appears to initially decrease to a minimum ≈40 min into charge (3.74 V), before increasing; this minimum corresponds to the maximum value in the *c* lattice parameter. The oxygen positional parameter also reaches a maximum value in conjunction with minimum values for the lattice parameters at the charged state (arrow in Figure 10). These changes in the structure (maxima in *c* lattice parameter and oxygen position during charge) are entirely consistent with the structural changes seen in the computational results as the Na content decreases (as discussion in Section 2.7).

In order to consolidate these findings, sequential multiphase Rietveld refinements were performed in a systematic manner attempting to account for the phase transitions observed. It should be noted that the reliability of the lattice parameters is excellent; as with any in situ or complex structural refinement, determination of the atomic parameters is slightly less reliable. For the sequential analysis the following steps were taken. From the beginning, the original phase (Phase 1) was modeled with sodium, oxygen, and lattice parameters varying until 6.8 min or 3.50 V, then these parameters were fixed at the last refined values. For the 11.2 to 28.8 min region, Phase 2 was introduced and the phase fractions of Phases 1 and 2, as well as the Phase 2 lattice, sodium and oxygen parameters were refined until 28.8 min (3.62 V). The refinement of the Phase 2 parameters was continued into the following solid solution region until 59.6 min or 3.97 V. Near the charged state, from 64 to 94.8 min or 4.06 V on charge and to 2.96 V on discharge, two phases were modeled (Phases 2 and 3) and their sodium content, oxygen positional parameter, phase fractions, and lattice parameters were refined. Thus, this approach models the simultaneous two-phase and solid solution reactions where both phases vary with time, i.e., it captures the solid solution and two-phase changes of these components. Note the region between 86 to 94.8 min or 3.25 to 2.95 V was particularly problematic to model as the lattice and phase fractions were correlated and the phases jumped between lattice parameters. Here various approaches were trialed, including fixing one phase and refining various components in only one phase, and determining the correlation between atomic and lattice parameters. For the final part of discharge from 2.70 to 1.50 V, the lattice parameters were fixed at those found from the refinements shown in **Table 4** (from the last discharged dataset). The culmination of these processes is shown in **Figure 11** and the fitting statistics of the sequential refinements are presented in Table S1 in the Supporting Information.

Ex situ XRD analysis of extracted electrodes cycled at C/2.5 were also conducted for the charged and discharged states. As per the discussion in the Supporting Information, the quality of the collected data is significantly better with the in situ synchrotron XRD. In addition, the batteries had to be stopped,

Table 4. Refined crystallographic parameters for Phase 2, $Na_{0.80(3)}Fe_{2/3}Mn_{1/3}O_2$, and Phase 3, $Na_{0.52(2)}Fe_{2/3}Mn_{1/3}O_2$ at the last dataset on discharge (121 min, 1.50 V).

Atom	Wyckoff	x	y	z	SOF[a)]	Isotropic ADP[a)] [×100)/Å^2]
Phase 2						
Na	3	0	0	0	0.80(3)	17.1[b)]
Mn	3	0	0	0.5	1/3	7.86[b),c)]
Fe	3	0	0	0.5	2/3	7.86[b),c)]
O	6	0	0	0.240(1)	1	7.63[b)]
Phase 3						
Na	3	0	0	0	0.52(2)	16.4[b)]
Mn	3	0	0	0.5	1/3	7.92[b),c)]
Fe	3	0	0	0.5	2/3	7.92[b),c)]
O	6	0	0	0.2289(9)	1	7.49[b)]

[a)]Atomic displacement parameter (ADP), site occupancy factor (SOF); [b)]Refined alternatively to SOFs and fixed for this region see Table 3; [c)]Constrained to be equal. Space group = *R*-3*m*, 30 refinement parameters, χ^2 = 1.49, R_p = 1.66%, wRp = 2.17%, Phase 2 *a* = 2.9426(5), *c* = 16.6302(6) and weight fraction of 48.8(3)% and Phase 3 Å *a* = 2.9294(3), *c* = 16.4894(8) Å and weight fraction of 51.2(2)%.

extracted and dried prior to ex situ analysis. During this process, the structure can be modified from the C/2.5 state, via electrode relaxation. The results indicate a loss of signal strength at the charged state which is also observed in the in situ data (Figure 1), and preservation of the O3-type structure at the discharged state but with lattice parameters corresponding to those of the charged state Phase 3 from the in situ data. In contrast, a two-phase mixture was found at the discharged state with the in situ data. This suggests equilibration occurs in the electrode during extraction from the cell, especially considering the high cycling rates used. In order to improve resolution of the ex situ XRD data, the electrodes could be removed from the current collectors, packed into capillaries and examined using high resolution ex situ synchrotron XRD; this will be undertaken in our future work, which will explore variable current rates and the reliability of ex situ XRD data for showing high rate phenomena.

2.7. Discussion of the Phase Evolution

The sodium content decreases during charge, as expected, and shows an overall increase during discharge. However, sodium content of the individual phases may differ from the overall sodium content of the electrode as the phase fractions need to be taken into account. At the charged state the total sodium content in the electrode is 0.27(20) taking into account the sodium occupancy in both phases and their phase weight fractions.

On charge, the *a* lattice parameter is shown to contract for all three phases and increase during discharge. The *c* lattice parameter increases initially on charge and then decreases, apparently reaching a maximum value. Comparing with in situ neutron powder diffraction data of layered oxides used as cathodes in lithium-ion batteries,[15a] for example, in Li(Ni,Mn,Co)O_2 (NMC) cathodes, the *c* lattice parameter, associated with the stacking axis of the layered structure, reaches a maximum value at the ≈70% state of charge while in $LiCoO_2$, Li(Ni,Co,Al)O_2 (CGR) cathodes, the *c* lattice stabilizes rather than reaching a maximum.[15a,16] The contraction in the Li(Ni,Mn,Co)O_2 cathode *c* lattice parameter is associated with some Li locating on the Ni site within the transition-metal layers. When the Li is removed or redistributed from the Ni layers in the structure (to the interlayer sites or out of the structure) the result is a reversal of the trend in the *c* lattice parameter (i.e., from expansion to contraction).[16] However, such a mechanism is unlikely in the $Na_{2/3}Fe_{2/3}Mn_{1/3}O_2$ process, but the observation of lattice expansion/contraction over a charge process is observed in other cathodes.

On charge, the oxygen positional parameter initially shows minor changes, but then increases, reaching values close to $x = y = z \approx 0.25$ for the fully charged state. The onset of the

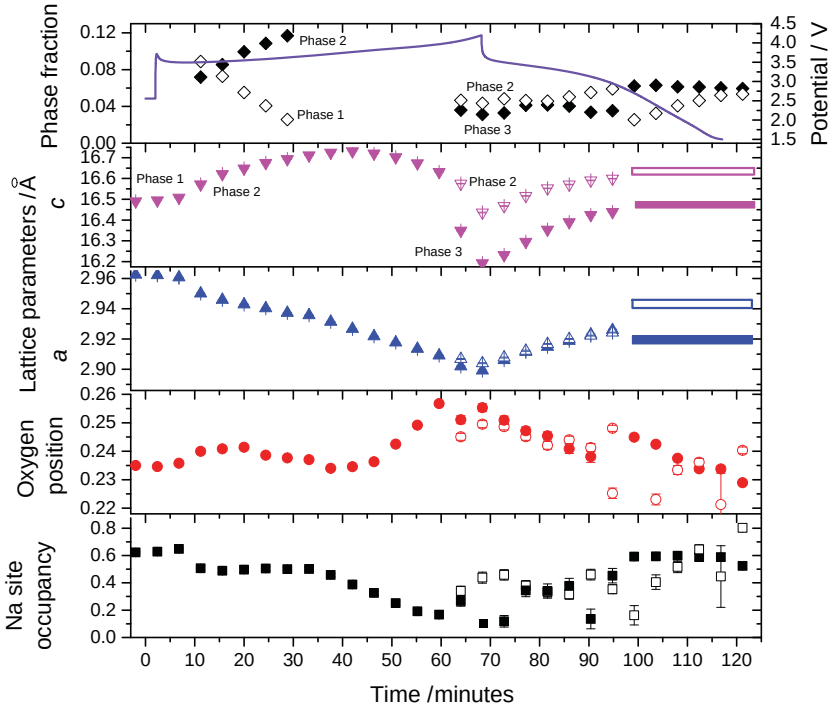

Figure 11. The evolution of the $Na_{0.622(6)}Fe_{2/3}Mn_{1/3}O_2$ electrode during charge/discharge. The *c* (purple triangles) and *a* (blue triangles) lattice parameters, oxygen positional parameter (red circles), sodium SOF (black squares), phase fractions (black diamonds), and the potential profile. When Phase 2 is introduced it is labeled and in the first two-phase reaction region Phase 1 phase fractions are modeled with open diamonds while Phase 2 is modeled with closed diamonds and the atomic parameters of Phase 2 is presented. Near the charged state and onward, open symbols represent Phase 2 and closed symbols represent Phase 3. The boxes for lattice parameters on discharge represent fixed lattice parameters.

increase corresponds to the decrease in the *c* lattice parameter (or maxima in the *c* lattice parameter during charge). The Fe/Mn–O bond lengths follow the same trend, decreasing from an initial value of 2.048(3) Å in the original cathode (Phase 1) to 2.036(1) Å, before increasing to 2.202(13) Å (Phase 3) and 2.161(13) Å (Phase 2) at the charged state. Again, the minimum corresponds to the maximum in the *c* lattice parameter. The initial decrease is expected, since the bond lengths should shorten as the charge on the central cation increases (e.g., Mn^{3+} becomes Mn^{4+} and Fe^{3+} becomes Fe^{4+}), resulting in stronger attraction of the O^{2-} to the central cation. The contraction of the *a* lattice parameter is also caused by this decreasing bond length. The increase in the bond length near the charged state is more surprising and future work will focus on understanding the cause. It may be related to Jahn–Teller distortions of the Mn^{3+} and Fe^{4+} octahedra and the structure attempting to facilitate this distortion (i.e., trying to average out the effect), while maintaining the Fe/Mn–O octahedral layers, which could result in an increase in the long-range (average) bond lengths. Interestingly, the calculations discussed below support these findings—as the Na content decreases (charge), the calculated bond lengths initially decrease but then increase at low Na content. In future work, ex situ X-ray absorption spectroscopy (XAS) and Mossbauer spectroscopy will be used to try to experimentally verify the bond length observations. However, as noted above, ex situ measurements do not always give direct correlation with in situ measurements at high cycling rates; ideally these experiments would be performed in situ for direct correlation.

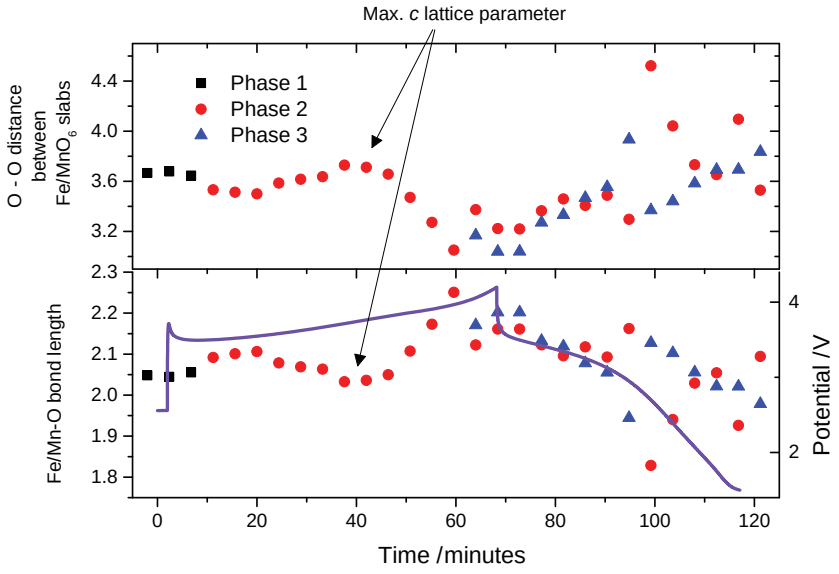

Figure 12. The evolution of the Fe/Mn–O bond lengths and O–O distances between the Fe/MnO_6 octahedral slabs or layers in Phase 1 (black squares), Phase 2 (red circles), and Phase 3 (blue triangles) during charge/discharge (potential curve also shown).

Thus, overall these data suggest a significant connection between the *c* lattice parameter, oxygen position and Fe/Mn–O bond lengths. These trends will be discussed in more detail below. On discharge the *a* and *c* lattice parameters increase, while the oxygen positional parameter decreases (overall) for both phases. The Na SOF shows an overall increase. Both phases appear to follow similar trends but show increase and decrease in phase fraction relative to each other.

The other important distance to compare in these materials is the distance between the layers. In Phase 1 in the original cathode, the distance between two equivalent O atoms in two adjacent layers is 3.667(6) Å, in Phase 3 at the charged state it is 3.04(3) Å, in Phase 2 at the charged state it is 3.22(3) Å and at the maximum in the *c* lattice parameter at 42 min it is 3.712(1) Å in Phase 2. Thus, the interlayer spacing follows the same trend as the *c* lattice parameter, increasing to a maximum on charge before decreasing. On charge the Mn/Fe–O layers are initially repelled from each other due to O–O repulsion; as Na is removed the overall negative charge on the Mn/Fe–O layers repel each other. However, as the sodium content decreases further, this repulsion is overcome and the layers collapse, due to the lack of interlayer Na; this collapse of the layers begins at 3.77 V or 42 min.

To visually demonstrate this connection, the Fe/Mn–O bond lengths and O–O distances between the Fe/MnO_6 octahedral layers is shown in **Figure 12** for each Phase during charge/discharge. Essentially, the bond lengths and interlayer distance remain fairly stable until ≈40 min into charge (3.74 V) when the *c* lattice parameter is at a maximum. Following this point the layers come closer together and the Fe/Mn–O bond lengths appear to lengthen substantially until the charged state. If we consider that the majority of first charge to be the Fe^{3+} to Fe^{4+} couple, the feature observed ≈40 min (3.74 V) on charge is likely to be a result of the formation of sufficient quantities of Jahn–Teller active Fe^{4+} and the structure is attempting to compensate for the local requirements of such cations. During discharge the bond lengths and interlayer spacing in both Phase 2 and Phase 3 appear to return toward the original values, although there is more scatter in the data on discharge.

Electrochemically the charge capacity was ≈127 mAh g^{-1} and the discharge capacity 170 mAh g^{-1}; this differs by 5%–10% compared to a fresh cell cycled at the C/10 rate[9] and the difference can be ascribed to the cell construction conditions (e.g., materials and in situ compared to conventional coin cells). The potential profile (e.g., Figure 2) shows a lack of major potential plateaus. This supports the notion that either solid-solution or multiple two-phase and solid-solution reactions occur in the electrode. If there were only two-phase reactions they would produce potential plateaus and this electrode appears to show a variable potential profile, and thus shows that multiple reactions occur simultaneously with regions of solely single-phase reactions. Importantly the O3 structural motif is maintained throughout the charge/discharge process.

2.8. Comparison with Literature and Calculations

Literature provides limited evidence for the sequence of phase transitions of the O3 phase in related O3 systems.[17] Some evidence exists of phase transitions on charge from the O3 phase to a monoclinic O1 phase followed by a rhombohedral P3 phase and in some cases a monoclinic P1 phase or an OP2 phase.[9, 14] On discharge, the electrode appears to undergo two-phase and solid solution reactions and does not necessarily recover the original phase.[9] For O3 $Na(Ni_{1/3}Fe_{1/3}Mn_{1/3})O_2$, it has been found by ex situ XRD that the O3 structure is maintained after 150 cycles.[17b] The O3 $Na_{2/3}Fe_{2/3}Mn_{1/3}O_2$ at the C/2.5 rate appeared to maintain an O3-type structure throughout the charge/discharge process. The results presented here indicate that solid-solution and two-phase transitions occur during the electrochemical process of O3-$Na_{2/3}Fe_{2/3}Mn_{1/3}O_2$, but the structural motif and space-group is preserved. It is important to note that the C/2.5 current rate presented here is relatively high and highly unusual in the literature where common in situ experiments can be of the order of C/50. These much slower rates may give different phase transformation behavior from the faster rates used to test electrochemical performance. This rate-dependent phase transformation behavior may explain the apparent discrepancy between electrochemical performance and phase stability for O3-$Na_{2/3}Fe_{2/3}Mn_{1/3}O_2$. The phase stability of the O3 phase observed in this work, where structural analysis has been performed in situ using a fast rate, may account for the similar electrochemical performance of this phase to the equivalent P2-phase and other systems.[9]

A recent parallel study on O3-$Na_xFe_{2/3}Mn_{1/3}O_2$ using laboratory-based *operando* and "relaxed," and ex situ synchrotron XRD data[18] can be critically compared with our observations. The comparison supports the discussion above. First, the data in our work is at the C/2.5 rate, significantly higher than the C/50-C/80 rates used in the reported study. Although the data presented in our work is also *operando*, the quality of the data allowed us to use Rietveld analysis for our structural models. This gives a direct quantification of the atomic, in particular sodium, parameters with respect to the charge-discharge of the electrode at these high rates. The reported work modeled the lattice parameters using Le Bail methods in the in situ experiments and used ex situ (extracted electrodes) for full structural (Rietveld) characterization.[18] As demonstrated above relaxation at higher rates makes such ex situ approaches unreliable. However, use of lower rates meant there was a focus on the equilibrium structures[18] while our work focuses on more kinetic, nonequilibrium phenomena. Interestingly these authors first discharged the electrode, inserted sodium to reach Na ≈ 0.96 before charging or extracting sodium, while our work charges first, extracts sodium. The reported work found a combination of phase transition during charge, from O′3, O3, P3 and then the P-type phase moves to O-type. Furthermore, the O3 phase persists within the P3-type region and is hypothesized to transform to O1.[18] Our starting composition $Na_{0.622(6)}Fe_{2/3}Mn_{1/3}O_2$ falls in the O3 range and we do not observe the O′3 phase which was found at higher Na concentrations in the reported work. Additionally, from the reported Mössbauer and XAS details[18] it is only the Fe^{3+}/Fe^{4+} couple that should be active in our work during charge. Our work solely observes the O3 phase which was described as persistent at C/80 rates even through the P3-type region (which the authors attributed to inhomogeneity in the electrode).[18] Speculatively, the higher rates employed in our work may not provide sufficient time for the P3 phase to nucleate leaving only the O3-type phase. At higher rates (C/2.5) the O3 model is found until the charged state while complex phase transitions are observed in the C/80 rate near the charged state related to the environment of the remaining sodium between the MO_6 layers.[18] Notably, the slab distance evolution shown in Figure 12 shows a very similar maxima at Na = 0.5 in the reported study, where sodium content determined from electrochemical charge passed through the cell[18] while we observe the maxima at Na = 0.39 noting that our sodium content is determined from Rietveld analysis. Similarity in the *c* lattice parameter evolution is also found in both studies. The combination of the results presented here and the work undertaken at C/80 rates provides unique insights into the function of this material.

To gain more insight into the structural evolution, and given that ex situ measurements are not able to give this insight directly, static energy minimization calculations were conducted where the structural properties (lattice parameters, oxygen position parameter, and Fe/Mn–O bond lengths) for the O3 phase were calculated as a function of Na content. The results show that, as the Na content decreases, the *c* lattice parameter initially increases while *a* decreases, the oxygen position parameter decreases and the Fe/Mn–O bond length decreases. These changes are all in agreement with the experimental results (Figures 10–12). As mentioned earlier, the initial increase in the *c* lattice parameter may be related to increasing repulsion between Mn/Fe–O layers due to the stronger O–O repulsion as Na is removed from between the layers. As stated earlier, a decrease in the Fe/Mn–O bond length and *a* lattice parameter is expected due to the stronger attraction with the increased Fe/Mn charge. The initial decrease in the oxygen position parameter appears to be a natural consequence of the increasing *c* lattice parameter, exaggerated by the decreasing Fe/Mn–O bond length during this initial part of charge.

When the Na content is reduced on further charge, significant changes in the structure occur. The *c* lattice parameter drops suddenly, as the amount of Na is no longer enough to keep the layers apart. Simultaneously, the oxygen position parameter increases to ≈0.25 and the Fe/Mn–O bond length increases. This is in line with the observations from the experiments (Figures 11 and 12). The computational results show that the *a* lattice parameter increases at these low sodium contents which is not observed experimentally; however, the magnitude of the changes in the *a* lattice parameter are small relative to changes in the other parameters. The decrease in the calculated *c* lattice parameter is significantly larger than that observed in the experiments. This may be due to there being a slightly uneven distribution of Na ions in the materials. Indeed, calculations for which some sites have a Na partial occupancy just above 0.18 and others have a partial occupancy just below 0.18 show intermediate values for the *c* lattice parameter. However, these results do suggest that the Na content is unlikely to reach as low as zero; hence, a Na content of 0.18 was used for the refinement of Phase 3 at the charged state.

Finally, the calculated energy of the O3 structure is less than the P2 structure for all values of Na content from 1.0 until 0.18. This is consistent with the experimental observation that no transformation to the P2 structure occurs and that the likely Na concentration in Phase 3 is close to 0.18. The significant changes in transitioning from O3 to P2 are also found in the literature.[5,6c]

3. Conclusion

Using advanced high resolution time-resolved in situ synchrotron XRD experiments, the structural evolution of O3 $Na_{2/3}Fe_{2/3}Mn_{1/3}O_2$ has been analyzed at C/2.5 and it is shown that the O3-type phase is maintained through charge and discharge. However, a sequence of solid-solution and two-phase transitions is observed as the Na content is varied (charge/discharge of the cell). Interestingly we characterize regions with simultaneous solid-solution and two-phase transitions, in particular where two phases are undergoing both types of reactions. The persistent crystal structure motif may account for the observed electrochemical performance of this electrode, which has been found to be similar to that of the P2 phase that is known to have good structural stability.

With these in situ XRD measurements, we are able to model multiple phases and their lattice and atomic (e.g., Na SOF and O positional parameter) evolution during electrochemical charge/discharge inside a functioning coin cell battery. This level of detailed sheds atomic-scale insight on the electrochemical function. This work represents one of the first detailed sodium-centered structural studies at such high current rates. Since such high current rates were employed, computational studies were used to assist with the analysis; the computational studies agree with the experimental results regarding changes in the lattice parameters, oxygen position parameter and bond lengths, thus lending support to the proposed structural evolution during electrode function. However, further work is now required to understand the subtleties in the structural evolution, e.g., Fe/Mn–O bond length variations. The computational results were used to assign the Na content of the low-Na content phase, since this could not be confidently determined from the refinements. Additionally, these results suggest that this computational method can be used for related systems as a predictive tool.

4. Experimental Section

The O3-$Na_{2/3}Fe_{2/3}Mn_{1/3}O_2$ phase was synthesized using a stoichiometric mixture of $NaNO_3$, $Fe(OH)_3$, and $Mn(OH)_2$ pelletized and heated under 1 bar O_2 atmosphere at 700 and 900 °C successively for 1 h with intermediate grinding.[9] Electrode preparation was performed in an Ar-filled glove box in order to avoid any atmospheric moisture contamination. The electrode slurry was prepared by mixing an active material, super carbon C65, and polyvinylidene fluoride (PVdF) as a binder in the mass ratio of 80:10:10 in *N*-methyl-2-pyrrolidone (NMP) followed by vigorous stirring for 2 h. The slurry was then cast onto an aluminum current collector sheet using a minicoater. The laminate was immediately transferred into a vacuum oven and dried at 80 °C under constant vacuum for 12 h.

Half coin cells with 3 mm diameter holes in the casing and 5 mm diameter holes in the stainless steel spacer were used for the construction of the coin cells for the in situ measurements. The coin cells contained Na metal (≈1 mm thickness), glass fiber separator with 0.5 M $NaPF_6$ in ethylene carbonate and dimethyl carbonate (1:1 wt%) electrolyte solution. In situ synchrotron X-ray diffraction experiments were performed within 1–2 d after cell construction. Further details regarding coin cell construction and beamline setup can be found in our previous publications.[11a,b,19]

In situ synchrotron XRD data were collected on the Powder Diffraction beamline[20] at the Australian Synchrotron with a wavelength (λ) of 0.68829(2) Å, determined using the NIST 660a LaB_6 standard reference material. Data were collected continuously in 4.4 min acquisitions on the coin cell in transmission geometry throughout the charge/discharge cycles. The coin cells were first charged to 4.2 V at 0.2 mA and then discharged to 1.5 V at 0.2 mA. This corresponds to C/2.5 on charge and discharge (≈100 mA g^{-1}). Note the electrochemical processes were started 2 min after the synchrotron XRD data collection. Rietveld refinements were carried out using the GSAS[21] software suite with the EXPGUI[22] software interface. Details of the ex situ XRD procedure are presented in the Supporting Information.

The structural properties of $Na_xFe_{2/3}Mn_{1/3}O_2$ were investigated as a function of x using static energy minimization calculations as implemented in the GULP code.[23] This approach is based on the classical Born model of ionic solids, which assumes that ions interact by long-range Coulombic interactions and short-range Pauli repulsion and van der Waals forces. A shell model was used to include ion polarizabilty.[24] Buckingham potentials were used to model the short-range interactions. The interatomic potential parameters were taken from Cherry et al.[25] for Fe^{3+}, Mn^{3+}, and O^{2-}, Mather et al.[26] for Fe^{4+}, Jackson and Catlow[27] or Na^+ and Kovaleva et al.[28] for Mn^{4+}. A cutoff of 12 Å was used for the short-range interactions. All Na and metal cation sites were treated as being partially occupied, by the appropriate proportions of Mn^{4+}, Mn^{3+}, Fe^{4+}, and Fe^{3+} in the case of the latter. Calculations for all structures included a full optimization of all lattice parameters and atomic positions with no symmetry constraints.

Supporting Information

Supporting Information is available from the Wiley Online Library or from the author.

Acknowledgements

The authors would like to thank undergraduate UNSW students Laura Jeffress, Damian Goonetilleke, and Emily Cheung for assistance during the in situ synchrotron XRD experiments. James C. Pramudita would like to thank UNSW/ANSTO for the Ph.D. Scholarship. Neeraj Sharma would like to thank AINSE Ltd for providing support through the research fellowship scheme. Part of this research was undertaken on the Powder Diffraction beamline at the Australian Synchrotron, Victoria, Australia. CIC Energigune work was financially supported by Ministerio de Economía y Competitividad (Proyecto I+D. Retos 2013), Reference Nos. ENE 2013–44330-R and FPDI-2013–17329, and the Gobierno Vasco/EuskoJaurlaritza (Etortek CICEnergigune 10, SAIOTEK-12 ENERGIBA and IT570–13).

Received: April 23, 2015
Revised: May 29, 2015
Published online: July 6, 2015

[1] J. B. Goodenough, Y. Kim, *Chem. Mater.* **2010**, *22*, 587.
[2] R. K. Evans, *Energy* **1978**, *3*, 379.

[3] S. R. Taylor, *Geochim. Cosmochim. Acta* **1964**, *28*, 1273.
[4] a) V. Palomares, P. Serras, I. Villaluenga, K. B. Hueso, J. Carretero-Gonzalez, T. Rojo, *Energy Environ. Sci.* **2012**, *5*, 5884; b) V. Palomares, M. Casas-Cabanas, E. Castillo-Martinez, M. H. Han, T. Rojo, *Energy Environ. Sci.* **2013**, *6*, 2312; c) M. H. Han, E. Gonzalo, G. Singh, T. Rojo, *Energy Environ. Sci.* **2015**, *8*, 81.
[5] C. Delmas, J.-J. Braconnier, C. Fouassier, P. Hagenmuller, *Solid State Ionics* **1981**, *3/4*, 165.
[6] a) J.-J. Braconnier, C. Delmas, P. Hagenmuller, *Mater. Res. Bull.* **1982**, *17*, 993; b) A. Maazaz, C. Delmas, P. Hagenmuller, *J. Inclusion Phenom.* **1983**, *1*, 45; c) A. Mendiboure, C. Delmas, P. Hagenmuller, *J. Solid State Chem.* **1985**, *57*, 323; d) M. H. Han, E. Gonzalo, M. Casas-Cabanas, T. Rojo, *J. Power Sources* **2014**, *258*, 266; e) N. Yabuuchi, M. Kajiyama, J. Iwatate, H. Nishikawa, S. Hitomi, R. Okuyama, R. Usui, Y. Yamada, S. Komaba, *Nat. Mater.* **2012**, *11*, 512.
[7] C. Delmas, C. Fouassier, P. Hagenmuller, *Phys. B* **1980**, *99B*, 81.
[8] D. H. Lee, J. Xu, Y. S. Meng, *Phys. Chem. Chem. Phys.* **2013**, *15*, 3304.
[9] E. Gonzalo, M. H. Han, J. M. Lopez del Amo, B. Acebedo, M. Casas-Cabanas, J. M. Rojo, *J. Mater. Chem. A* **2014**, *2*, 18523.
[10] a) N. Sharma, V. K. Peterson, M. M. Elcombe, M. Avdeev, A. J. Studer, N. Blagojevic, R. Yusoff, N. Kamarulzaman, *J. Power Sources* **2010**, *195*, 8258; b) N. Sharma, G. Du, A. J. Studer, Z. Guo, V. K. Peterson, *Solid State Ionics* **2011**, *199*, 37; c) N. Sharma, M. V. Reddy, G. Du, S. Adams, B. V. R. Chowdari, Z. Guo, V. K. Peterson, *J. Phys. Chem. C* **2011**, *115*, 21473; d) N. Sharma, X. Guo, G. Du, Z. Guo, J. Wang, Z. Wang, V. K. Peterson, *J. Am. Chem. Soc.* **2012**, *134*, 7867; e) N. Sharma, V. K. Peterson, *J. Solid State Electrochem.* **2012**, *16*, 1849; f) N. Sharma, V. K. Peterson, *Electrochim. Acta* **2013**, *101*, 79; g) N. Sharma, V. K. Peterson, *J. Power Sources* **2013**, *244*, 695; h) N. Sharma, D. Yu, Y. Zhu, Y. Wu, V. K. Peterson, *Chem. Mater.* **2013**, *25*, 754; i) N. Sharma, M. Wagemaker, in *Neutrons Applications in Materials for Energy* (Eds.: V. K. Peterson, G. J. Kearley), Springer, Heidelberg, **2015**, pp. 139–204.
[11] a) P. Serras, V. Palomares, T. Rojo, H. E. A. Brand, N. Sharma, *J. Mater. Chem. A* **2014**, *2*, 7766; b) N. Sharma, P. Serras, V. Palomares, H. E. A. Brand, J. Alonso, P. Kubiak, M. L. Fdez-Gubieda, T. Rojo, *Chem. Mater.* **2014**, *25*, 4917; c) J. C. Pramudita, S. Schmid, T. Godfrey, T. Whittle, M. Alam, T. Hanley, H. E. A. Brand, N. Sharma, *Phys. Chem. Chem. Phys.* **2014**, *15*, 24178.
[12] R. Berthelot, D. Carlier, C. Delmas, *Nat. Mater.* **2011**, *10*, 74.
[13] J. C. Pramudita, R. D. Aughterson, W. M. Dose, S. W. Donne, H. E. A. Brand, N. Sharma, *J. Mater. Res.* **2014**, *30*, 381.
[14] a) M. Sathiya, K. Hemalatha, K. Ramesha, J.-M. Tarascon, A. S. Prakash, *Chem. Mater.* **2012**, *24*, 1846; b) S. Komaba, N. Yabuuchi, T. Nakayama, A. Ogata, T. Ishikawa, I. Nakai, *Inorg. Chem.* **2012**, *51*, 6211.
[15] a) M. Alam, T. Hanley, W. K. Pang, V. K. Peterson, N. Sharma, *Powder Diffr.* **2014**, *29*, S35; b) H. Liu, F. C. Strobridge, O. J. Borkiewicz, K. M. Wiaderek, K. W. Chapman, P. J. Chupas, C. P. Grey, *Science* **2014**, *344*, 1252817.
[16] O. Dolotko, A. Senyshyn, M. J. Muhlbauer, K. Nikolowski, H. Ehrenberg, *J. Power Sources* **2014**, *255*, 197.
[17] a) X. Li, D. Wu, Y.-N. Zhou, L. Liu, X. Q. Yang, G. Ceder, *Electrochem. Commun.* **2014**, *49*, 51–54; b) D. Kim, E. Lee, M. Slater, W. Lu, S. Rood, C. S. Johnson, *Electrochem. Commun.* **2012**, *18*, 66.
[18] B. Mortemard de Boisse, J.-H. Cheng, D. Carlier, M. Guignard, C.-J. Pan, S. Bordere, D. Filimonov, C. Drathen, E. Suard, B. J. Hwang, A. Wattiaux, C. Delmas, *J. Mater. Chem. A* **2015**, *3*, 10976.
[19] a) W. R. Brant, S. Schmid, G. Du, Q. Gu, N. Sharma, *J. Power Sources* **2013**, *244*, 109; b) G. Du, N. Sharma, J. A. Kimpton, D. Jia, V. K. Peterson, Z. Guo, *Adv. Funct. Mater.* **2011**, *21*, 3990; c) R. J. Gummow, N. Sharma, R. Feng, G. Han, Y. He, *J. Electrochem. Soc.* **2013**, *160*, A1856.
[20] K. S. Wallwork, B. J. Kennedy, D. Wang, *AIP Conf. Proc.* **2007**, *879*.
[21] A. C. Larson, R. B. Von Dreele, Los Alamos National Laboratory Report LAUR 86–748, **1994**.
[22] B. H. Toby, *J. Appl. Cryst.* **2001**, *34*, 210.
[23] a) J. D. Gale, A. L. Rohl, *Mol. Simul.* **2003**, *29*, 291; b) J. D. Gale, *J. Chem. Soc., Faraday Trans.* **1997**, *93*, 629.
[24] B. G. Dick, A. W. Overhauser, *Phys. Rev.* **1958**, *112*, 90.
[25] M. Cherry, M. S. Islam, C. R. A. Catlow, *J. Solid State Chem.* **1995**, *118*, 125.
[26] G. C. Mather, M. S. Islam, F. M. Figueiredo, *Adv. Funct. Mater.* **2007**, *17*, 905.
[27] R. A. Jackson, C. R. A. Catlow, *Mol. Simul.* **1988**, *1*, 207.
[28] N. N. Kovaleva, J. L. Gavartin, A. L. Shluger, A. V. Boris, A. M. Stoneham, *J. Exp. Theor. Phys.* **2002**, *94*, 178.